Published on 11 January 2018. Downloaded by WUHAN UNIVERSITY OF TECHNOLOGY on 20/04/2018 03:53:16.

ChemComm

COMMUNICATION

View Article Online
View Journal | View Issue

Check for updates

Cite this: *Chem. Commun.*, 2018, **54**, 1469

Received 21st November 2017,
Accepted 11th January 2018

DOI: 10.1039/c7cc08959g

rsc.li/chemcomm

Stepwise chelation-etching synthesis of carbon-confined ultrafine SnO_2 nanoparticles for stable sodium storage†

Yuanjie Zhang,[a] Jiashen Meng,[a] Xuanpeng Wang,[a] Xiong Liu,[a] Xiaoming Xu,[a] Ziang Liu,[a] Kwadwo Asare Owusu,[a] Congyun Huang,[b] Qi Li*[a] and Liqiang Mai *[a]

A stepwise chelation-etching approach to synthesize carbon-confined ultrafine SnO_2 nanoparticles was developed *via* conformal coating with polydopamine and chelation-etching with ethylenediaminetetraacetic acid (EDTA). EDTA plays a crucial role in the ordered removal of cobalt and tin. The obtained composite exhibits superior sodium storage performance.

The eagerness for renewable energy resources and the urgent demand for low-cost energy storage have stimulated rising interest and much research on sodium-ion batteries (SIBs), due to the abundant sodium resource in the earth's crust and even global distribution.[1–3] Developing electrode materials with high specific capacity, long cycling stability and excellent rate capability is highly desired. Among all the anodes for SIBs, SnO_2 and its derivatives stand out because of their prominent theoretical capacity (1378 mA h g^{-1}), abundant natural resource and low cost.[3–5] However, SnO_2-based anodes suffer from multiple problems, such as unstable cycling performance and poor rate capability, due to the intrinsic low conductivity and large volume change during cycling.[6,7]

Many efforts have been devoted to addressing the aforementioned issues of SnO_2 anodes. Typically, one effective strategy is to fabricate the SnO_2 anodes with novel architectures, such as hollow and porous structures, which can accommodate the volume change and keep their structural integrity.[8–10] Another method is to combine SnO_2 with carbon materials, such as SnO_2/graphene composites,[11–13] SnO_2/carbon nanotube composites,[14,15] *etc.* The introduced carbon materials can alleviate the structural destruction from volume fluctuation and improve the electronic transport property of anode materials. Another popular method is the synthesis of nanosized SnO_2. Nanoscale materials can contribute to increasing the active sites and the contact area between anode and electrolyte, supporting fast ion diffusion, relieving stress and improving mechanical stability.[10–13,15,16] In addition, it is believed that N-doped carbon can increase the electronic conductivity of materials and thus enhance the electrochemical performance.[17,18] Therefore, well-designed carbon-confined SnO_2 nanostructures are highly desirable to obtain superior electrochemical performance.

Herein, we have developed a stepwise chelation-etching strategy to synthesize carbon-confined ultrafine SnO_2 nanoparticles (SnO_2@NC) *via* conformal coating with polydopamine and chelation-etching with EDTA. The chelation-etching of EDTA with metal ions is crucial in the controlled synthesis of SnO_2@NC composites. The obtained composites are composed of ultrafine SnO_2 nanocrystals with a high specific surface area and plenty of mesopores confined in conductive N-doped carbon boxes. All of these merits contribute to the superior electrochemical performance. The strategy to synthesize SnO_2@NC is schematically illustrated in Fig. 1. Firstly, uniform $CoSn(OH)_6$ nanocubes with side length of about 100 nm (Fig. S1, ESI†) were synthesized *via* a co-precipitation method.[19] Then, the pre-prepared $CoSn(OH)_6$ was successively coated with dopamine, which was employed as an N-doped carbon source because of its versatile conformal coating, facile synthesis process and relatively high yield of N-doped carbon.[20] Then, $CoSn(OH)_6$@polydopamine

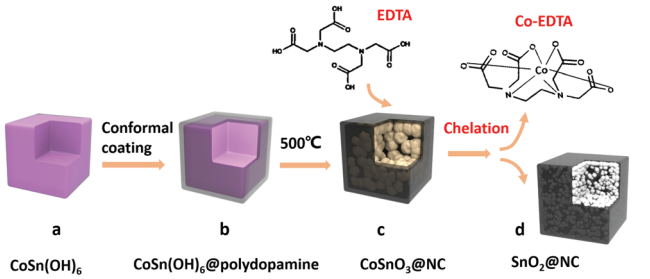

Fig. 1 Schematic illustration of the stepwise chelation-etching strategy to synthesize carbon-confined ultrafine SnO_2 nanoparticles.

[a] *State Key Laboratory of Advanced Technology for Materials Synthesis and Processing, Wuhan University of Technology, Wuhan 430070, Hubei, China. E-mail: qi.li@whut.edu.cn, mlq518@whut.edu.cn*

[b] *School of Materials Science and Engineering, Wuhan University of Technology, Wuhan 430070, Hubei, China*

† Electronic supplementary information (ESI) available: Experimental details and supplementary figures. See DOI: 10.1039/c7cc08959g

Published on 11 January 2018. Downloaded by WUHAN UNIVERSITY OF TECHNOLOGY on 20/04/2018 03:53:16.

nanocubes were calcined at 500 °C in nitrogen, thus forming $CoSnO_3$@N-doped carbon nanocubes ($CoSnO_3$@NC) composed of bulks and cracks (Fig. S2a, ESI†), which are clearly observed in the transmission electron microscope (TEM) images (Fig. S2c and d, ESI†). Subsequently, EDTA is crucially chosen as the chelation-etching agent to remove the metal ions of $CoSnO_3$@NC during the hydrothermal chelation process, forming ultrafine SnO_2 nanoparticles confined in the N-doped carbon boxes with abundant mesopores. By varying the EDTA concentration, a series of SnO_2@NC products is obtained. The as-prepared samples are denoted as SnO_2@NC-1, SnO_2@NC-1.2, SnO_2@NC-1.5 and SnO_2@NC-2 to correspond with a molar ratio of EDTA to $CoSnO_3$@NC of 1, 1.2, 1.5 and 2, respectively.

The effects of different EDTA concentrations on the products were monitored by several characterization methods. When the molar ratio was 1, all the peaks of the as-prepared sample in the X-ray powder diffraction (XRD) pattern could be indexed to pure SnO_2 (Fig. 2a, JCPDS No. 01-077-0447). The scanning electron microscope (SEM) images show the well-maintained cubic shape of the starting material with uniform size (Fig. S3a, ESI†), which is consistent with the TEM images (Fig. 2b). From the high-resolution TEM (HRTEM) images (Fig. 2c), it can be seen that the bulks of $CoSnO_3$@NC have transformed to nanoparticles. The selected-area electron diffraction (SAED) pattern shows the polycrystalline nature of the SnO_2@NC-1 and the diffraction rings can be assigned to the SnO_2 phases (Fig. 2d). Inductively coupled plasma atomic emission spectrometry (ICP-AES) of SnO_2@NC-1 (Table S1, ESI†) further confirmed that only trace amounts of cobalt remain after chelation. All the above facts imply that the cobalt of $CoSnO_3$@NC has been substantially chelated by EDTA and so SnO_2@NC is formed, which leads to a higher mass loss of 21.7% (Fig. S4, ESI†) compared to 9.3% (Fig. S2b, ESI†) for $CoSnO_3$@NC, as shown by thermogravimetric analysis (TGA),

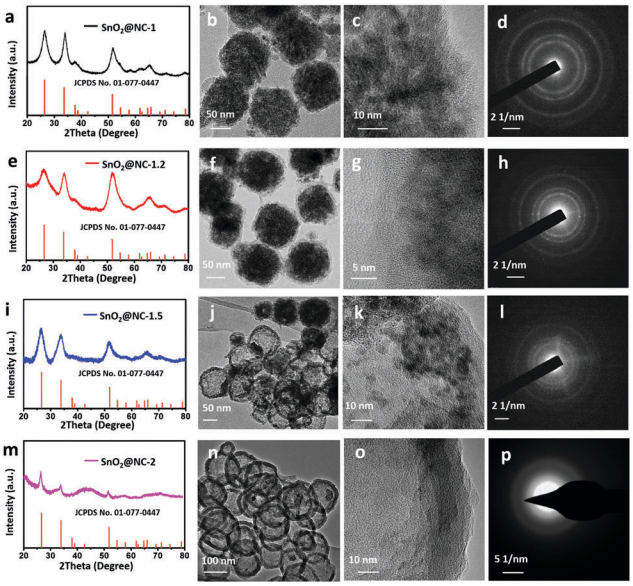

Fig. 2 (a, e, i and m) XRD patterns, (b, f, j and n) TEM images, (c, g, k and o) HRTEM images and (d, h, l and p) SAED patterns of SnO_2@NC-1 (a–d), SnO_2@NC-1.2 (e–h), SnO_2@NC-1.5 (i–l) and SnO_2@NC-2 (m–p).

indicating the increase of carbon content. As the molar ratio was increased to 1.2, the as-prepared sample was still the pure SnO_2 phase (Fig. 2e). However, the TEM image (Fig. 2f) and the HRTEM image (Fig. 2g) show that the inner nanoparticles have become slightly smaller in size and more porous compared to SnO_2@NC-1, indicating that EDTA started to chelate tin, thus leading to a higher mass loss of 23.6% (Fig. S4, ESI†), as shown by TGA. As the molar ratio was increased to 1.5, the TEM image (Fig. 2j) and the HRTEM image (Fig. 2k) show that the inner nanoparticles have become more sparse as well as smaller in size compared to SnO_2@NC-1.2, implying that EDTA chelated tin further and this gives rise to a higher mass loss of 28.6%, as shown by TGA (Fig. S4, ESI†). The SEM images (Fig. S3b and c, ESI†) show almost undifferentiated morphology, and SAED patterns (Fig. 2h and l) verify the same polycrystalline nature of the SnO_2@NC-1.2 and SnO_2@NC-1.5. As the molar ratio was increased to 2, only three major peaks of SnO_2, with low intensity, are observed in the XRD pattern (Fig. 2m), which implies a very low content of SnO_2 and is further confirmed by a high mass loss of 73.9%, as shown by TGA (Fig. S4, ESI†). The morphology of SnO_2@NC-2 is well-maintained (Fig. S3d, ESI†). However, the corresponding TEM image (Fig. 2n) and HRTEM image (Fig. 2o) show virtually hollow carbon boxes with no observable inner core in most carbon boxes, which is further confirmed by the SAED pattern (Fig. 2p). This suggests that tin has been substantially chelated by EDTA. According to previous reports,[21,22] cobalt(II) and tin(IV) can react with EDTA to form a 1 : 1 complex. On the basis of the above discussions, we deduce that EDTA first chelates the cobalt of $CoSnO_3$@NC *via* the reaction shown in eqn (1). After the chelation of cobalt, EDTA starts to chelate the tin of SnO_2 as displayed in eqn (2). (To clearly illustrate the reaction process, EDTA is denoted as H_4Y^{4-}, taking no account of its hydrolysis.)

$$H_4Y^{4-} + CoSnO_3 \rightarrow [CoY^{4-}]^{2-} + SnO_2 + H_2O + 2H^+ \quad (1)$$

$$H_4Y^{4-} + SnO_2 \rightarrow SnY^{4-} + 2H_2O \quad (2)$$

The textural properties of the composites before ($CoSnO_3$@NC) and after (SnO_2@NC) chelation were evaluated by N_2 adsorption/desorption isotherms, as depicted in Fig. S5 (ESI†). The composites before and after chelation all exhibit a type IV isotherm with a H4 hysteresis loop characteristic of mesoporous materials (Fig. S5, ESI†). The Brunauer–Emmett–Teller (BET) specific surface areas of $CoSnO_3$@NC and SnO_2@NC-1 are 75 and 129 $m^2\,g^{-1}$, respectively (Fig. S5f, ESI†). The increase in specific surface area should be due to EDTA chelation, leading to the transformation from bulks to nanoparticles. The pore sizes of $CoSnO_3$@NC and SnO_2@NC-1 are 11 and 2.5 nm, respectively (Fig. S5f, ESI†). The decrease in pore size can be ascribed to the disappearance of cracks and the formation of mesopores. With increasing ratio, the BET specific surface area of the final products increases gradually for SnO_2@NC-1.2 and SnO_2@NC-1.5 but decreases for SnO_2@NC-2 (Fig. S5f, ESI†). This occurrence may result from the further EDTA chelation. With EDTA addition and chelation of tin, the number of SnO_2 nanoparticles increases, while the size decreases, leading to the

 This journal is © The Royal Society of Chemistry 2018

Published on 11 January 2018. Downloaded by WUHAN UNIVERSITY OF TECHNOLOGY on 20/04/2018 03:53:16.

increase of surface area. When tin is chelated further and the content of nanoparticles decreases dramatically, the surface area decreases accordingly.

To further confirm the chelation reaction, the colour change in the synthesis process was recorded (Fig. S6, ESI†). As EDTA chelates specific metal ions and forms coordination bonds, the colour of the chelate would deepen compared to the specific colour of the metal ion. The Co^{2+} ion has a clear light red colour in aqueous solution (Sn^{4+} ion is colourless), while the colour of the solution after chelation turns aubergine, which is strong evidence of a chelation reaction. Then, Fourier transform infrared (FTIR) spectroscopy was performed for EDTA and the aubergine chelate of SnO_2@NC-1.2 (Fig. S7, ESI†). The peak at 3018 cm^{-1} in the spectrum of EDTA is assigned to the stretching vibration of the C–H band in the CH_2 groups of the EDTA molecule.[23] However, it shifts to 2983 cm^{-1} in the spectrum of the aubergine chelate, which is strong evidence for the formation of a chelate as previously reported by Sawyer.[21] The other prominent peak at 1650 cm^{-1} in the spectrum of the aubergine chelate is due to the C=O stretching of the carboxylate group (COO^-) in EDTA chelates, which is regarded as an indication of the formation of a metal–carboxylate coordination bond.[24]

To give more insight into the SnO_2@NC-1.2, further analyses were carried out on the sample. The SEM images (Fig. 3a and b) and the TEM image (Fig. 3c) show that the cubic shape of the $CoSn(OH)_6$ precursor is well maintained after calcination and chelation. As shown in the HRTEM image (Fig. 3d), there are small SnO_2 nanoparticles with an appropriate size of about 5 nm encapsulated inside the porous carbon layer with a uniform thickness of about 7 nm. The interplanar spacing is 0.35 nm (Fig. 3e), corresponding to the (110) plane of SnO_2. The SAED pattern (Fig. 3f) shows the polycrystalline nature and the diffraction rings from inside to outside can match well with the (110), (211) and (101) lattice planes, respectively. Energy-dispersive X-ray spectroscopy (EDS) mapping images (Fig. 3g) confirm the uniform distribution of O, Sn, N and C elements. The Raman spectrum (Fig. S8, ESI†) demonstrates that the outer carbon layers are partly graphitized. The full X-ray photoelectron spectroscopy (XPS) survey spectrum (Fig. S9a, ESI†) shows the existence of C, N, O and Sn in SnO_2@NC-1.2, which is consistent with the EDS mapping results. The spectrum of Sn 3d (Fig. S9b, ESI†) is divided into two peaks that are located at 486.1 eV and 494.5 eV and can be assigned to Sn $3d_{5/2}$ and Sn $3d_{3/2}$, respectively, demonstrating that Sn atoms are in the form of SnO_2.[25] The high resolution N 1s spectrum (Fig. S9c, ESI†) indicates the presence of four different types of nitrogen species bonded to carbon.[17] The high resolution C 1s spectrum (Fig. S9d, ESI†) shows the high percentage of graphitic carbon, suggesting the partly graphitized nature of the carbon layer.[17]

The sodium storage performances of SnO_2@NC-1, SnO_2@NC-1.2 and SnO_2@NC-1.5 have been evaluated. Fig. 4a and Fig. S10 (ESI†) show the discharge/charge voltage profiles. All three curves share the same charging and discharging voltage slope but show different initial specific capacities. SnO_2@NC-1.2 demonstrates an initial specific capacity of 1097 mA h g^{-1}, but SnO_2@NC-1 and SnO_2@NC-1.5 exhibit specific capacities of 796 and 875 mA h g^{-1}, respectively, indicating that SnO_2@NC-1.2 shows the highest initial discharge capacity. The curves exhibit slopes instead of constant voltage plateaus partially due to the nanosize effect.[14,26] The smooth slope observed at 1.2 V in the initial discharge, which is absent in subsequent cycles, is due to the formation of a solid electrolyte interphase (SEI).[25] Gradient changes of the slopes are observed at 1.25 and 0.5 V in the charge and

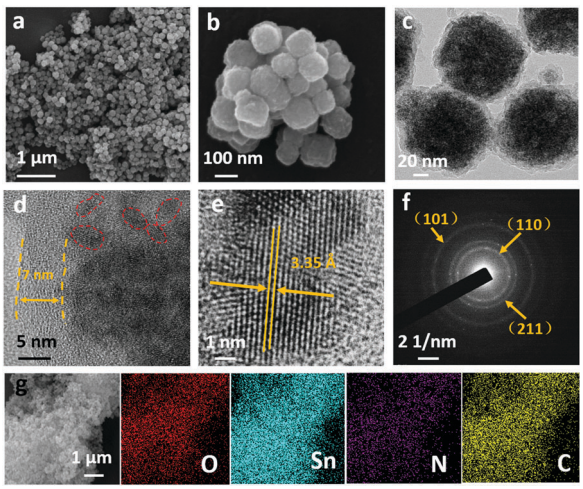

Fig. 3 (a and b) SEM images, (c) TEM image, (d and e) HRTEM images, (f) SAED pattern and (g) SEM and corresponding elemental mapping images of SnO_2@NC-1.2.

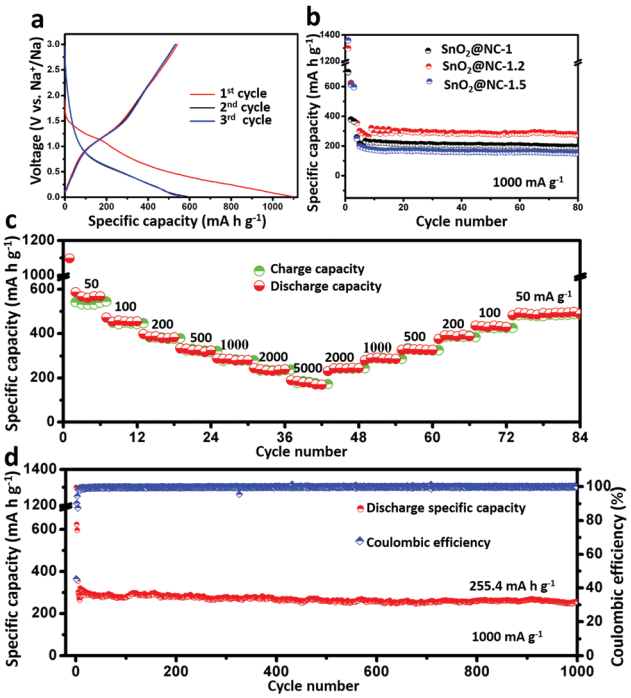

Fig. 4 (a) Charge–discharge profiles of SnO_2@NC-1.2 at a current density of 50 mA g^{-1}; (b) cycling performance of SnO_2@NC at a current density of 1000 mA g^{-1}; (c) rate performance of SnO_2@NC-1.2; (d) long cycling performance of SnO_2@NC-1.2 and corresponding coulombic efficiency at a current density of 1000 mA g^{-1}. (The electrodes in (b) and (d) were activated at a current density of 50 mA g^{-1} for the first three cycles.)

Published on 11 January 2018. Downloaded by WUHAN UNIVERSITY OF TECHNOLOGY on 20/04/2018 03:53:16.

discharge curves, respectively, which are attributed to reversible reactions between SnO_2 and Na ions,[14] in agreement with the CV results (Fig. S11, ESI†). Fig. 4b shows that all the electrodes exhibit stable cycle performances after activation but different discharge capacities. SnO_2@NC-1, SnO_2@NC-1.2 and SnO_2@NC-1.5 demonstrate discharge capacities of 194.6, 278.5 and 151.1 mA h g^{-1}, respectively, at a current density of 1000 mA g^{-1} after 80 cycles. SnO_2@NC-1.2 obtains a higher capacity than the other two electrodes. Fig. 4c shows that the average discharge capacities for SnO_2@NC-1.2 are 570, 455, 384, 323, 285, 236 and 180 mA h g^{-1} at the current densities of 50, 100, 200, 500, 1000, 2000 and 5000 mA g^{-1}, respectively. Compared to SnO_2@NC-1 and SnO_2@NC-1.5 (Fig. S12, ESI†), SnO_2@NC-1.2 delivers a much higher capacity at each current density. Electrochemical impedance spectroscopy measurements (Fig. S13, ESI†) also show that SnO_2@NC-1.2 has the lowest transfer resistance. Furthermore, the SEM images obtained after cycling show that the morphology of the SnO_2@NC composites is generally preserved without serious aggregation (Fig. S14, ESI†). When SnO_2@NC-1.2 was cycled at 200 mA g^{-1}, a high stable discharge capacity of 380 mA h g^{-1} was achieved (Fig. S15, ESI†). Most impressively, at 1000 mA g^{-1}, SnO_2@NC-1.2 can still deliver 255.4 mA h g^{-1} after 1000 cycles with capacity retention of 84.9% compared to the fifth cycle (Fig. 4d). When the current density is increased to 2000 mA g^{-1}, it still exhibits a superior discharge capacity and very stable cycling (Fig. S16, ESI†). The sodium storage performance of SnO_2@NC-1.2, in terms of cycling stability and rate capability, is superior to previously reported SnO_2-based anodes (Table S2, ESI†), suggesting the effectiveness of our method.

The superior sodium storage performance of SnO_2@NC-1.2 can be ascribed to the following aspects: (1) ultrafine SnO_2 nanoparticles formed *via* chelation can provide plenty of active sites, a high surface area and a short diffusion distance for a good electrochemical reaction; (2) chelation of cobalt and tin can generate small-sized nanoparticles with void space between them, which can accommodate the volume variation of SnO_2 and maintain the structural integrity; (3) the N-doped carbon boxes encapsulating the ultrafine SnO_2 nanoparticles can improve the conductivity and avoid aggregation.

In summary, a novel and efficient approach to synthesize SnO_2@NC was developed *via* conformal coating with polydopamine and chelation-etching with EDTA. It has been demonstrated that EDTA chelates cobalt first followed by tin. When the molar ratio of EDTA to $CoSnO_3$@NC is 1.2, the as-prepared SnO_2@NC shows the best sodium storage performance and delivers a high reversible specific capacity (570 mA h g^{-1} at 50 mA g^{-1}), excellent rate capability (180 mA h g^{-1} at 5000 mA g^{-1}) and stable cycling performance (255.4 mA h g^{-1} at 1000 mA g^{-1} after 1000 cycles). This novel synthesis route may be extended to other metal oxides (Fig. S17, ESI†) and paves a new way to synthesize carbon-confined ultrafine nanoparticles for high energy storage.

This work was supported by the National Key Research and Development Program of China (2016YFA0202603), the Programme of Introducing Talents of Discipline to Universities (B17034), the National Natural Science Foundation of China (51521001) and the State Key Laboratory of Advanced Technology for Materials and Processing at Wuhan University of Technology (2016-KF-1). We thank Prof. Xiangfeng Duan of University of California, Los Angeles, for strong support and stimulating discussions.

Conflicts of interest

There are no conflicts to declare.

Notes and references

1 M. D. Slater, D. Kim, E. Lee and C. S. Johnson, *Adv. Funct. Mater.*, 2013, **23**, 947–958.
2 J. Y. Hwang, S. T. Myung and Y. K. Sun, *Chem. Soc. Rev.*, 2017, **46**, 3529–3614.
3 J. Cui, S. Yao and J. K. Kim, *Energy Storage Mater.*, 2017, **7**, 64–114.
4 C. Bommier and X. Ji, *Isr. J. Chem.*, 2015, **55**, 486–507.
5 Y. Kim, K. Ha, S. Oh and K. Lee, *Chem. – Eur. J.*, 2014, **20**, 11980–11992.
6 J. Huang, L. Zhong, C. Wang, J. P. Sullivan, W. Xu, L. Zhang, S. Mao, N. S. Hudak, X. Liu, A. Subramanian, H. Fan, L. Qi, A. Kushima and J. Li, *Science*, 2010, **330**, 1515–1520.
7 M. Gu, A. Kushima, Y. Shao, J. Zhang, J. Liu, N. D. Browning, J. Li and C. Wang, *Nano Lett.*, 2013, **13**, 5203–5211.
8 Y. Hong, M. Son and Y. Kang, *Adv. Mater.*, 2013, **25**(2279–2283), 2250.
9 C. Han, B. Zhang, K. Zhao, J. Meng, Q. He, P. He, W. Yang, Q. Li and L. Mai, *Chem. Commun.*, 2017, **53**, 9542–9545.
10 X. Zhou, L. Yu and X. Lou, *Adv. Energy Mater.*, 2016, **6**, 1600451.
11 D. Su, H. J. Ahn and G. Wang, *Chem. Commun.*, 2013, **49**, 3131–3133.
12 Y. Wang, Y. Lim, M. Park, S. Chou, J. Kim, H. Liu, S. Dou and Y. Kim, *J. Mater. Chem. A*, 2014, **2**, 529–534.
13 L. Pei, Q. Jin, Z. Zhu, Q. Zhao, J. Liang and J. Chen, *Nano Res.*, 2014, **8**, 184–192.
14 J. Cui, Z. Xu, S. Yao, J. Huang, J. Huang, S. Abouali, M. A. Garakani, X. Ning and J. K. Kim, *J. Mater. Chem. A*, 2016, **4**, 10964–10973.
15 Y. Wang, D. Su, C. Wang and G. Wang, *Electrochem. Commun.*, 2013, **29**, 8–11.
16 P. Meduri, E. Clark, E. Dayalan, G. U. Sumanasekera and M. K. Sunkara, *Energy Environ. Sci.*, 2011, **4**, 1695.
17 X. Xie, D. Su, J. Zhang, S. Chen, A. K. Mondal and G. Wang, *Nanoscale*, 2015, **7**, 3164–3172.
18 H. Li and H. Zhou, *Chem. Commun.*, 2012, **48**, 1201–1217.
19 Z. Wang, Z. Wang, H. Wu and X. Lou, *Sci. Rep.*, 2013, **3**, 1391.
20 Y. Liu, K. Ai and L. Lu, *Chem. Rev.*, 2014, **114**, 5057–5115.
21 D. Sawyer and P. Paulsen, *J. Am. Chem. Soc.*, 1959, **81**, 816–820.
22 J. Kragent, *Talanta*, 1975, **22**, 505–510.
23 L. Bellamy, *Russian Translation*, 1963, 111.
24 D. Busch and M. Morris, *J. Am. Chem. Soc.*, 1956, **78**, 5178–5181.
25 L. Fan, X. Li, B. Yan, J. Feng, D. Xiong, D. Li, L. Gu, Y. Wen, S. Lawes and X. Sun, *Adv. Energy Mater.*, 2016, **6**, 1502057.
26 M. Okubo, E. Hosono, J. Kim, M. Enomoto, N. Kojima, T. Kudo, H. Zhou and I. Honma, *J. Am. Chem. Soc.*, 2007, **129**, 7444–7452.

 This journal is © The Royal Society of Chemistry 2018